Biophysical Journal
Article

Biophysical Society

Coherent Timescales and Mechanical Structure of Multicellular Aggregates

Miao Yu,[1] Aria Mahtabfar,[2] Paul Beelen,[2] Yasir Demiryurek,[1] David I. Shreiber,[3] Jeffrey D. Zahn,[3] Ramsey A. Foty,[2] Liping Liu,[1,4] and Hao Lin[1,*]

[1]Department of Mechanical and Aerospace Engineering, Rutgers, The State University of New Jersey, Piscataway, New Jersey, [2]Department of Surgery, Rutgers Robert Wood Johnson Medical School, New Brunswick, New Jersey, [3]Department of Biomedical Engineering, and [4]Department of Mathematics, Rutgers, The State University of New Jersey, Piscataway, New Jersey

ABSTRACT Multicellular aggregates are an excellent model system to explore the role of tissue biomechanics in specifying multicellular reorganization during embryonic developments and malignant invasion. Tissue-like spheroids, when subjected to a compressive force, are known to exhibit liquid-like behaviors at long timescales (hours), largely because of cell rearrangements that serve to effectively dissipate the applied stress. At short timescales (seconds to minutes), before cell rearrangement, the mechanical behavior is strikingly different. The current work uses shape relaxation to investigate the structural characteristics of aggregates and discovers two coherent timescales: one on the order of seconds, the other tens of seconds. These timescales are universal, conserved across a variety of tested species, and persist despite great differences in other properties such as tissue surface tension and adhesion. A precise mathematical theory is used to correlate the timescales with mechanical properties and reveals that aggregates have a relatively strong envelope and an unusually "soft" interior (weak bulk elastic modulus). This characteristic is peculiar, considering that both layers consist of identical units (cells), but is consistent with the fact that this structure can engender both structural integrity and the flexibility required for remodeling. In addition, tissue surface tension, elastic modulus, and viscosity are proportional to each other. Considering that these tissue-level properties intrinsically derive from cellular-level properties, the proportionalities imply precise coregulation of the latter and in particular of the tension on the cell-medium and cell-cell interfaces.

INTRODUCTION

Three-dimensional (3D) cellular aggregates are an important and broadly applied model system for the study of a wide variety of biological processes including morphogenesis, carcinogenesis, malignant invasion, wound healing, and tissue engineering (1–6). Similar to real tissues, tissue-like aggregates are known to exhibit liquid-like properties (7–12). According to (5), "Behaviors which duplicate those of ordinary immiscible liquids include: 1) the rounding-up of irregularly-shaped tissue fragments toward a spherical shape, which serves to minimize surface area, and consequently, the amount of free energy of the system; 2) the spreading of one tissue mass over another to approach a particular anatomical configuration; 3) the sorting-out of heterotypic cell mixtures to approach the same anatomical configuration adopted by spreading; 4) the approach to the same final anatomic configuration by both cell sorting and tissue fusion; 5) the hierarchical ranking of a tissues' tendency to envelop another; and 6) the perfect correspondence between envelopment hierarchy and measured 'surface tension'." These liquid-like properties are predicated on one hand, by large-scale tissue flow realized via cell rearrangements (13–16), and on the other by the tissues' effective viscosity, which can be used to quantify the dissipative process (17–20). Also similar to a liquid, a "surface tension" arises from the energy difference between bulk and surface cells (vis-à-vis molecules) (21–24). This liquid analogy is even valid on a subtler level: when an aggregate (drop) composed of identical cells is compressed, cells (molecules) occupying an internal position exploit the compressing energy and move to the surface (19,25), effectively increasing surface area, dissipating the applied force, and minimizing the overall energy (26–28).

The above parallelism is true, however, only when considering the long-timescale (hours) behavior of tissues (5,12,29). This timescale is largely determined by that of the so-called T1 transition, the basic motion of cell rearrangement (20). Many studies are dedicated to understanding this

Submitted October 10, 2017, and accepted for publication April 9, 2018.

*Correspondence: hlin@soe.rutgers.edu

Editor: Mark Alber.

https://doi.org/10.1016/j.bpj.2018.04.025

phenomenon as well as measuring the long-time mechanical properties such as elastic moduli, effective viscosity, and surface tension (30–37). In particular, a recent study revealed a well-conserved rearrangement velocity of 1.8 μm/min (20). In contrast, the short-time mechanical behaviors of cell aggregates receive relatively little attention but may nevertheless be of equal importance (38). Put simply, short-time responses determine how stresses are distributed "immediately" after a mechanical exposure and set the stage for the long-time, liquid-like rearrangements that ensue. This is the focus of the current study.

We perform aggregate compression tests using a tissue surface tensiometer (TST) for a variety of aggregate types to analyze the shape-relaxation dynamics upon removal of the compressive force and apply a precise mathematical theory (39) to analyze the mechanical structure of the aggregate. We demonstrate the presence of two persistent timescales across all types: a short one on the order of a few seconds, and a long one on the order of a minute. Mechanically, the aggregates approximate a "hard envelope surrounding a soft bulk," in which the bulk elasticity is unusually weak, with the free mechanical energy mostly stored in the enveloping layer. This result is consistent with Krieg et al. (40), in which much stronger cortices were observed for cells on the surface in comparison with those in the aggregate interior. Such a structure requires that tissue has both strong structural integrity and necessary flexibility. The relevant mechanical properties follow proportionality with the surface tension, indicating strong regulation of the underlying cellular properties, including cortical tension and cell-cell adhesion. These results have specific implications for physical mechanisms underlying embryonic development, cancer research, and tissue engineering, and for a general understanding of emulsion and material synthesis.

MATERIALS AND METHODS

Cell lines

Five cell lines, one of which was tested under various drug/extracellular matrix (ECM) treatment conditions, were employed in this study. LN2a and LN4 cells were generated by transfecting noncohesive L929 cells (CCL-1; ATCC, Manassas, VA) with an N-cadherin expression vector (41), followed by fluorescence activated cell sorting using an automated single-cell-deposition system. LN2a and LN4 are clonal populations that are identical in every respect but with different levels of cell-surface N-cadherin: LN4 expresses ~2.5-fold more N-cadherin on its surface than LN2a (42). Although able to adhere to substrates, LN2a and LN4 cells only use cadherins to cohere to one another. Therefore, the shape-relaxation data are only dependent on cadherin-mediated cohesion. 3T3 (CRL-1658; ATCC) and Rat2 (CRL-1764; ATCC) are mouse and rat embryonal fibroblasts, respectively. Fibroblasts make collagens, glycosaminoglycans, reticular and elastic fibers, fibronectins, and other ECM proteins whose composition and function change when cells are placed in 3D culture or in response to a differentiation signal. Full exposition of the ECM environment in 3T3 and Rat2 cells is well beyond the scope of this study. Suffice it to say that the ECM is likely complex and differs between fibroblast lines. Glioblastoma multiforme (GBM) cells were developed from primary human glioblastoma brain tumor samples under a Rutgers IRB protocol (#CINJ 001208) and were characterized in (43) and (44). Previous studies demonstrated that GBM cells are responsive to various drugs that can significantly alter their cohesive and mechanical properties. GBM cells were treated with 0.1 μM dexamethasone (Dex) or 1 μM of the MEK inhibitor PD0325901 or dimethyl sulfoxide (DMSO) as vehicle control for 24 h before formation of hanging drop cultures. Dex treatment of GBM cells gives rise to an increase in fibronectin matrix assembly and to the reorganization of actin into stress fibers (43), whereas treatment with PD0325901 results only in actin-stress-fiber formation (45). These processes play a critical role in establishing aggregate mechanical properties; fibronectin matrix assembly engenders an increase in tissue cohesion (43) and stiffness, whereas actin is mainly involved in stiffening of both single cells and 3D aggregates (45). Drug treatment was also performed in combination with either 100 or 300 μg/mL of human fibronectin, as this has previously been shown to significantly influence tissue biomechanics (46). The GBM/drug/fibronectin combination treatments allow us to determine whether our model is able to detect subtle changes in tumor mechanical properties in response to drug treatment.

Generation of cellular spheroids

3D cellular aggregates were generated using the hanging drop method (47). Briefly, cells were detached by ethylenediaminetetraacetic acid, washed, and suspended at a concentration of 2.5×10^6 cells/mL in complete medium supplemented with 2 mM $CaCl_2$. 10 μL hanging drops were created by depositing cell droplets on the underside of a tissue culture dish lid and inverting the lid over its base, which contained 5 mL of phosphate-buffered saline for hydration. After 48 h of incubation under tissue culture conditions, aggregates that had formed at the base of each drop were transferred to agarose-coated 24-well dishes and further incubated until spheroid formation. Depending on the cell line and treatment, spheroids were ready within 24–72 h.

The resulting aggregates have a size ranging from 115 to 318 μm in radius. The radius is constrained to a lower limit that allows for compression of aggregates in the tensiometer (~100 μm) and an upper limit of 350 μm, beyond which aggregates develop a necrotic core because of reduced diffusion of growth factors and hypoxia of core cells. The size variation among the 12 aggregate types practically covers the whole range attainable with the current experimental setup.

Generation of shape-relaxation profiles

Compression and decompression of spheroids was performed in tissue culture medium at 37°C using a custom-built TST (8). Spherical cellular aggregates were loaded into the TST chamber and positioned between poly-(2 hydroxyethyl methacrylate)-coated parallel plates to which they cannot adhere. Compression was initiated by raising the lower plate until the aggregate contacted the upper plate, the degree of compression being varied through adjustment of the height of the lower plate. Aggregates were compressed for 30 s, whereupon the compressive force was removed and the aggregate was allowed to relax. A high-speed video camera (Lumenera Infinity 2 cooled CCD camera; Lumenera, Ottawa, Canada) was used to capture shape change during relaxation, which proceeded until the aggregate shape had approached sphericity. Additional study was performed with GBM2 aggregates (GBM cell line from another tumor sample) with varying compression times of 5, 10, 20, 30, 60, and 120 s to examine the dependence of shape-relaxation times on compression duration.

RESULTS

Aggregates were prepared following Materials and Methods. They were subject to compressions for 30 s with a TST

(except for the cases discussed in Appendix D, in which the dependence on compression time is studied) and allowed to relax upon removal of the compressing plate (see Video S1 for an example). An exemplary image is shown in Fig. 1 *a*. The relaxation process is recorded; the aggregate contour (*solid*) is extracted by a home-grown code, from which we calculate the centroid of the 2D shape and then use it as an approximation for the 3D centroid of the aggregate. The axis of symmetry (rotation) is determined to be perpendicular to the compressing plate and goes through the centroid. In this manner, we assume that the aggregate is an "oblate spheroid" (see Appendix A and Fig. 9 for volume verification and 3D shape extrapolation from the 2D contour) upon compression by the parallel plate. In a fashion similar to a Fourier transform, the resulting axisymmetric shape is then decomposed into axisymmetric spherical harmonics (corresponding to $m = 0$ in Laplace's spherical harmonics $Y_m^l(\theta,\phi)$, so that the ϕ-dependence is absent):

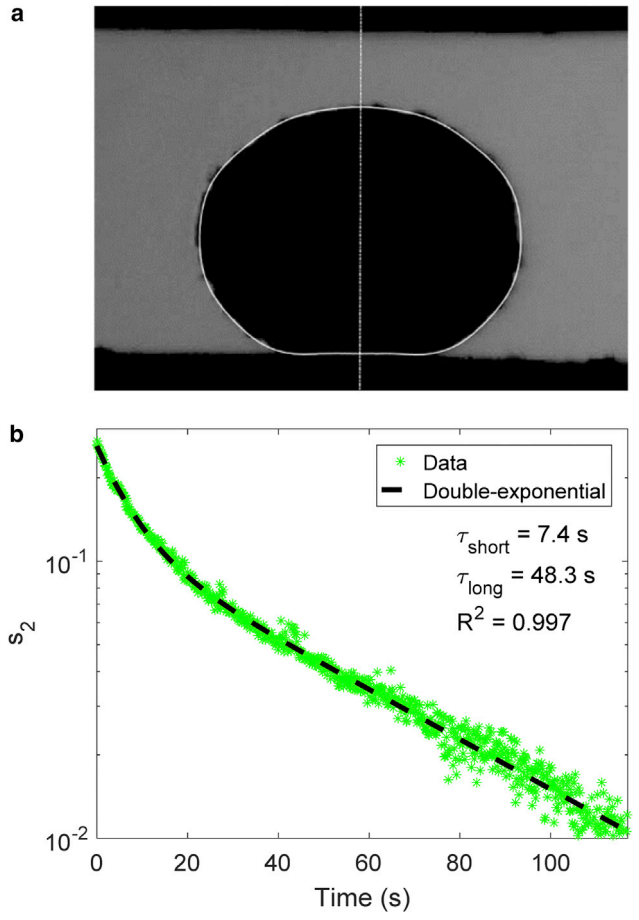

FIGURE 1 (*a*) Exemplary image of a GBM with DMSO aggregate during shape relaxation. The rectangular shapes in the image are the top and bottom plate of the TST, respectively. The contour (*solid*) is numerically extracted. The aggregate is assumed to be axisymmetric, and the axis (*dash-dot*) is calculated based on the contour. (*b*) The amplitude of the P_2 (*ellipsoidal*) mode, s_2, is shown as a function of time. The dashed is a double-exponential fitting per Eq. 2. To see this figure in color, go online.

$$r(\theta) \approx R\left(1 + f_{2,0}Y_0^2(\theta) + f_{3,0}Y_0^3(\theta) + \cdots + f_{10,0}Y_0^{10}(\theta)\right). \quad (1)$$

Here, $r(\theta)$ defines the 3D aggregate shape under the predefined polar coordinate system; R is the radius of equivalent volume; and $f_{l,0}$ is the magnitude of each spherical harmonics, Y_0^l. Mode Y_0^1 is not included because it corresponds to simple translation. Higher-order details ($l > 10$) are neglected in the fitted contour. The right-hand side in Eq. 1 defines an approximate axisymmetric 3D shape of the aggregate. To further improve shape analysis accuracy, we iterate the steps above. That is, we update the centroid using the 3D shape as defined by Eq. 1 and subsequently repeat all steps above until a convergence of both shape and centroid position is reached. Note that $Y_l^0(\theta)$ differs from the Legendre polynomial $P_l(\cos(\theta))$ by a constant factor. For convenience, we define $s_2 = (\sqrt{5/4\pi})f_{2,0}$ as the mode amplitude so that $s_2 P_2(\cos(\theta)) = f_{2,0}Y_0^2(\theta)$, where $P_2(x) = (3x^2 - 1)/2$. For a shape close to a spheroid,

$$s_2 \approx \frac{2}{3}\left(\frac{a}{b} - 1\right)$$

or

$$s_2 \approx \frac{4}{3}\frac{a-b}{a+b}$$

to the leading order, where a and b are the long and short semiaxis, respectively.

s_2 is quantified in temporal resolution as the main shape factor in this study. This choice is made because 1) P_2 mode is the most prominent mode in magnitude, which allows the best signal-to-noise ratio; and 2) according to the linear theory, different modes are decoupled from each other, and thus the solution to each mode can be achieved independently (39). Therefore, although the shape of aggregate can deviate from a sheer spheroidal shape upon plate compression, the analysis is not affected. In Fig. 1 *b*, s_2 is plotted as a function of time, where $t = 0$ corresponds to the beginning of shape relaxation. The data are very well captured by a double-exponential fitting in the form of

$$s_2(t) = Ae^{-t/\tau_{\text{short}}} + Be^{-t/\tau_{\text{long}}}, \quad (2)$$

from which the two timescales can be extracted. This form follows from (39). For the case shown, $\tau_{\text{short}} = 7.4$ s and $\tau_{\text{long}} = 48.3$ s. The second dominant mode, P_4, is in general not amenable to quantitative analysis because of a weak signal/noise ratio (Appendix B). τ_{short} and τ_{long} are found to be robust and have no dependence on the degree and the duration of compression (Figs. 11 and 12, respectively, in Appendix D). Furthermore, they demonstrate surprising consistency across the 12 types of aggregates we studied (Table 1). Because one is always on the order of seconds,

TABLE 1 Summary of Measured Properties for 12 Aggregate Types (Total $n = 290$)

Type	n	τ_{short} (s)	τ_{long} (s)	τ_{long}/τ_{short}	σ (mN/m)	R (μm)	$s_{2,max}$
LN2a	23	4.3 ± 1.5	51.8 ± 14.0	12.9 ± 3.4	2.43 ± 0.121	148 ± 22	0.193 ± 0.081
LN4	18	4.7 ± 1.2	42.6 ± 5.2	9.5 ± 2.3	5.62 ± 0.362	236 ± 19	0.216 ± 0.069
3T3	31	3.9 ± 1.6	45.5 ± 10.1	12.8 ± 4.6	20.1 ± 1.94	115 ± 15	0.176 ± 0.069
Rat2	21	3.6 ± 1.4	46.7 ± 9.6	14.5 ± 5.4	21.1 ± 1.42	151 ± 9	0.102 ± 0.044
GBM −Dex	23	6.1 ± 1.0	32.7 ± 2.4	5.5 ± 0.8	6.71 ± 0.589	318 ± 25	0.212 ± 0.046
GBM +Dex	32	4.9 ± 1.0	41.7 ± 7.6	8.6 ± 1.5	14.9 ± 0.803	254 ± 18	0.140 ± 0.042
GBM −Dex +300Fn	31	7.0 ± 3.1	43.9 ± 13.3	6.6 ± 1.4	7.90 ± 0.433	295 ± 26	0.222 ± 0.065
GBM +Dex +300Fn	19	3.5 ± 1.5	30.6 ± 10.9	9.5 ± 3.7	20.5 ± 0.936	290 ± 34	0.100 ± 0.030
GBM DMSO	24	8.4 ± 3.3	46.9 ± 11.4	6.1 ± 2.0	8.56 ± 0.441	282 ± 32	0.296 ± 0.052
GBM PD03	31	5.5 ± 1.7	42.8 ± 10.0	8.2 ± 2.6	9.53 ± 0.490	197 ± 42	0.256 ± 0.051
GBM DMSO +300Fn	22	4.6 ± 1.2	34.5 ± 5.3	7.8 ± 1.7	7.38 ± 0.455	281 ± 13	0.162 ± 0.041
GBM PD03 +300Fn	15	5.0 ± 0.8	39.3 ± 4.9	7.9 ± 0.8	35.3 ± 4.33	244 ± 4	0.140 ± 0.031

Abbreviations: GBM, glioblastoma; −Dex/+Dex, without and with dexamethasone treatment; +300Fn, with the addition of 300 μg/mL of soluble fibronectin (otherwise 100 μg/mL); DMSO, dimethyl sulfoxide treatment; PD03, treatment with the MAPK/ERK inhibitor PD0325901. The numbers represent mean and standard deviation, respectively.

and the other tens of seconds, we will denote them τ_{short} and τ_{long}, respectively, as in Eq. 2. They are analyzed in detail below.

Fig. 2 shows results for L cell aggregates, namely, LN2a ($n = 23$) and LN4 ($n = 18$). These cell lines are particularly interesting, as they are genetically engineered so that N-cadherin is their only source of adhesion, and the former expresses less than half (91,790 ± 3076) of surface cadherins per cell when compared with the latter (225,041 ± 7457) (42). Correspondingly, the surface tension, σ, approximately linearly correlates with the cadherin-expression level (Table 1). However, this correlation is not seen in the timescales. As shown in Fig. 2, $\tau_{short} = 4.3 \pm 1.5$ and 4.7 ± 1.2 s for LN2a and LN4, respectively, $p = 0.282$ (Welch's Test); $\tau_{long} = 51.8 \pm 14.0$ and 42.5 ± 5.2 s for LN2a and LN4, respectively, $p = 0.007$. The p-value for τ_{short} infers no statistically significant difference. For τ_{long}, the difference is significant yet is only weak in contrast to the proportionality in surface tension or surface cadherin density.

We next examine glioblastoma multiforme (GBM) aggregates. In prior work, we investigated the effects of various drugs on aggregate organization and dispersal, including the MAPK/ERK inhibitor PD0325901 (PD03), which was found to induce cell shape change and actin reorganization (45). When compared with the control group (DMSO, with the addition of 300 μg/mL of soluble fibronectin, denoted "+300Fn"), the PD03-treated aggregates have approximately a fivefold increase in surface tension (Table 1). However, Fig. 3 *a* indicates that $p = 0.185$ and 0.007 for τ_{short} and τ_{long}, respectively. Despite $p < 0.01$ for the latter, the mean value increases by only 13.9% under a fivefold increase in surface tension. A similar trend is observed for GBM aggregates with and without Dex treatment. Previous studies have shown that Dex treatment, by inducing fibronectin matrix assembly, significantly increased the strength of cell-cell cohesion, thereby inhibiting detachment of cells from the aggregate, reducing their dispersal and migration away from the primary mass in in vitro (43) and ex vivo (48) assays, and increasing aggregate surface tension by more than twice. This enhancement is more pronounced when cells are incubated with higher concentrations of fibronectin (Table 1). Again, the moderate differences in τ_{short} and τ_{long} (−19.7 and 27.5%, respectively) does not scale with the significant changes in the surface tension.

Taken together, all groups (see, in addition, GBM −Dex/+Dex +300Fn; GBM DMSO/PD03; and 3T3/Rat2 in Table 1) demonstrate a persistent robustness in the relaxation timescales despite significant changes in other properties. All timescales are presented in Fig. 4 against the aggregate surface tension, σ. The aggregate surface tension spans more than one order of magnitude, whereas the

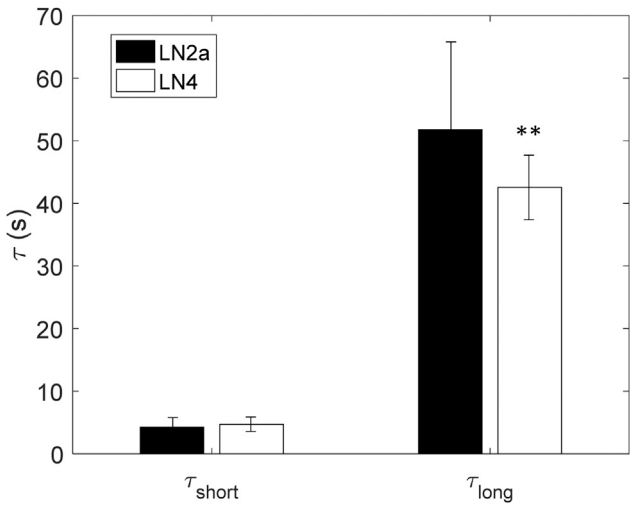

FIGURE 2 Relaxation times for LN2a and LN4 aggregates; the cell lines are genetically engineered to express different levels of N-cadherin, which leads to different aggregate surface tensions (Table 1). $\tau_{short} = 4.3 \pm 1.5$ and 4.7 ± 1.2 s for LN2a and LN4, respectively, $p = 0.282$. $\tau_{long} = 51.8 \pm 14.0$ and 42.5 ± 5.2 s for LN2a and LN4, respectively, $p = 0.007$. Error bars are SDs.

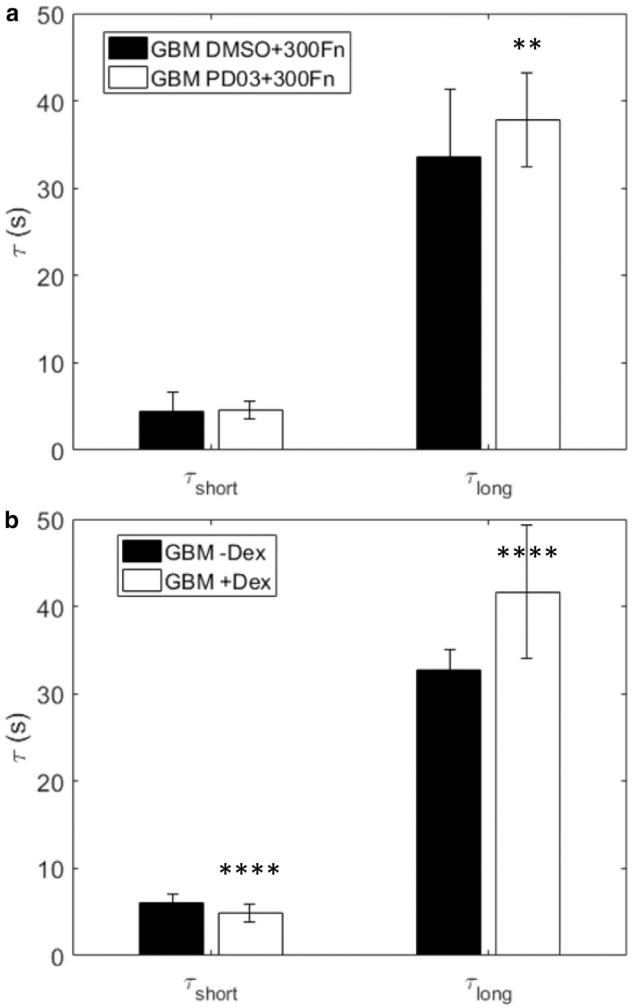

FIGURE 3 Relaxation times for GBM aggregates. (*a*) A comparison between control (DMSO) and PD03-treated groups, both with 300 μg/mL of soluble fibronectin (+300Fn), is shown. $\tau_{short} = 4.6 \pm 1.2$ s (DMSO) and 5.0 ± 0.8 s (PD03), $p = 0.185$; $\tau_{long} = 34.5 \pm 5.3$ s (DMSO) and 39.3 ± 4.8 s (PD03), $p = 0.007$. (*b*) A comparison between control (−Dex) and dexamethasone-treated (+Dex) groups is shown. $\tau_{short} = 6.1 \pm 1.0$ s (−Dex) and 4.9 ± 1.0 s (+Dex), $p = 4.20 \times 10^{-5}$. $\tau_{long} = 32.7 \pm 2.4$ s (−Dex) and 41.7 ± 7.6 s (+Dex), $p = 2.36 \times 10^{-7}$. Error bars are SDs.

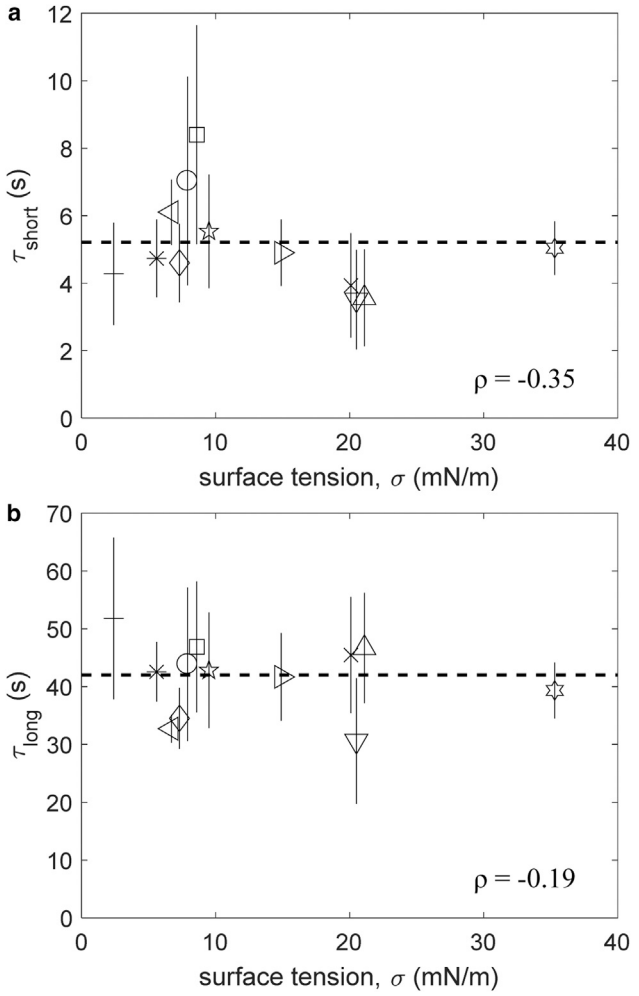

FIGURE 4 Relaxation times (short (*a*) and long (*b*)) versus surface tension for 12 types of aggregates. The aggregates (total $n = 290$), listed in Table 1, are as follows: LN2a (*plus sign*); LN4 (*asterisk*); 3T3 (*cross*); Rat2 (*upward-pointing triangle*); GBM DMSO (*square*); GBM3 PD03 (*pentagram*); GBM DMSO +300Fn (*diamond*); GBM PD03 +300Fn (*hexagram*); GBM −Dex (*left-pointing triangle*); GBM +Dex (*right-pointing triangle*); GBM −Dex +300Fn (*circle*); and GBM +Dex +300Fn (*downward-pointing triangle*). The Pearson correlation coefficient, ρ, is −0.35 between τ_{short} and σ and is −0.19 between τ_{long} and σ. Error bars are SDs. The variation in σ is in general small and not plotted for clarity.

relaxation timescales, averaging over all 12 groups (total $n = 290$), result in $\tau_{short} = 5.2 \pm 2.3$ and $\tau_{long} = 42.0 \pm 11.1$ s. The Pearson correlation coefficient, ρ, is −0.35 between τ_{short} and σ, and is −0.19 between τ_{long} and σ, suggesting weak linear correlations between both timescales and aggregate surface tension.

We then wished to determine if timescales correlated with aggregate size. We thus explored the relationship between the times and the aggregate radius, R. (The radius is that of a sphere with an equivalent volume.) Fig. 5 shows that τ_{short} is in general positively correlated with R ($\rho = 0.53$), whereas τ_{long} is in general negatively correlated with R ($\rho = -0.68$). On the other hand, when we plot τ_{long}/τ_{short} against $1/R$, a more evident trend stands out: this ratio of timescales is inversely correlated with the aggregate radius, R, or linearly correlated with $1/R$ (Fig. 6, *dashed*; $\rho = 0.84$, $R^2 = 0.71$ for a linear fit).

Theory

The above results are consistent with a model containing the presence of a surface entity different from the "bulk" (interior). For the current problem, an analytical solution can be achieved that is a special case of a more general solution obtained after prior work by four of us (L.L., M.Y., H.L., and R.A.F.) (39). Here, we provide a brief description of the governing equations and the boundary conditions. The

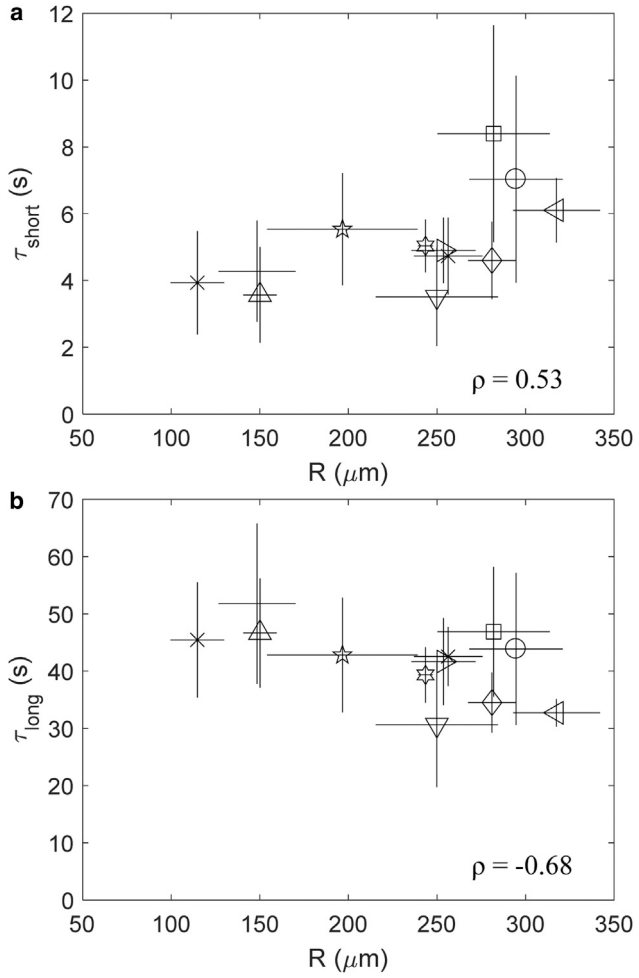

FIGURE 5 The timescales versus aggregate radius, R. The same description of symbols from Fig. 4 applies. Pearson correlation coefficient $\rho = 0.53$ and -0.68 for (a and b), respectively. All error bars are SDs.

aggregate bulk is modeled as a linear viscoelastic body described by a Kelvin-Voigt model:

$$\mathbf{T} = -p\mathbf{I} + \mu_b\left[\nabla\mathbf{u} + \nabla\mathbf{u}^T\right] + \eta\left[\nabla\dot{\mathbf{u}} + \nabla\dot{\mathbf{u}}^T\right].$$

Here $\mathbf{T}$ is the stress tensor, $\mathbf{u}$ is the displacement vector, p is the pressure field as a result of incompressibility (isovolumetric process), and $\mathbf{I}$ is the unit tensor. μ_b and η are bulk elastic modulus and viscosity, respectively, which are phenomenological parameters describing the rheological properties of the interior. The governing equations inside the aggregate are thus the stress balance condition

$$\nabla \cdot \mathbf{T} = 0,$$

along with continuity

$$\nabla \cdot \mathbf{u} = 0.$$

The medium outside the aggregate is ignored and pressure is set to ambient, p_0.

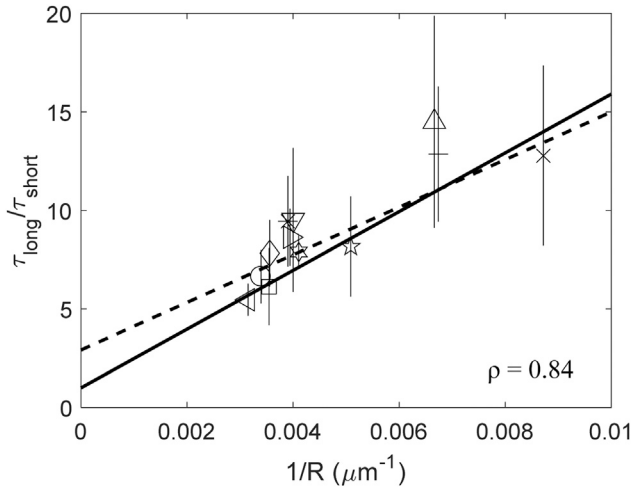

FIGURE 6 The ratio of times as a function of $1/R$. The dashed line is linear fit, $y = ax + b$, with $a = 1207$ μm and $b = 2.92$; $\rho = 0.84$, and the coefficient of determination $R^2 = 0.71$. The solid line is also a linear fitting, but we set $b = 1$ per Eq. 7. The coefficient of determination is 0.64. The same description of symbols from Fig. 4 applies. Error bars are SDs.

At the aggregate-medium interface, stress is continuous in both the normal and tangential directions,

$$\mathbf{n} \cdot \mathbf{T} = p_0 + 2\sigma H,$$

and

$$\mathbf{t} \cdot \mathbf{T} = 0,$$

where $\mathbf{n}$ and $\mathbf{t}$ are unit normal and tangential vector, respectively; σ is surface tension; and H is the mean curvature. Applying the governing equations and the boundary conditions on a spherical coordinate system and assuming small deformation (39) provides an exact solution in the form of double-exponential relaxation for each spherical harmonic (eigenfunctions of the partial differential equation system). For $s_2(t)$, the timescales defined in Eq. 2 are found to be

$$\tau_{short} = \left(\frac{20}{19}\frac{1}{\tau_1} + \frac{1}{\tau_2}\right)^{-1} \text{ and } \tau_{long} = \tau_2, \qquad (3)$$

where τ_1 and τ_2 are the two well-known apparent timescales in the viscoelasticity literature (49–52), defined by

$$\tau_1 = \frac{\eta R}{\sigma} \text{ and } \tau_2 = \frac{\eta}{\mu_b}. \qquad (4)$$

Equation 3 entails immediately that to observe double-exponential relaxation, i.e., two separate timescales of τ_{short} and τ_{long}, we necessarily have

$$\tau_1 \ll \tau_2, \quad \text{or } \tau_1 \sim \tau_2. \qquad (5)$$

This is because if the converse situation of $\tau_1 \gg \tau_2$ occurs, then $\tau_{short} \simeq \tau_{long}$, the two timescales collapse, and the double-exponential relaxation process becomes a single one. Because in our experiments, two timescales are always

clearly observable in each single case, and $\tau_{short} \ll \tau_{long}$, we arrive at

$$\frac{\sigma}{R} \gg \mu_b. \tag{6}$$

In other words, the surface is an envelope much "harder" than the interior.

We next examine the ratio of the timescales as predicted by the theory,

$$\frac{\tau_{long}}{\tau_{short}} = 1 + \frac{20}{19}\frac{\tau_2}{\tau_1} = 1 + \frac{20}{19}\left(\frac{\sigma}{\mu_b}\right)\frac{1}{R}. \tag{7}$$

This provides a form of correlation agreeable with Fig. 6. The intercept value 1 is somewhat lower than the fitted value of 2.92, and the linearity points to constancy of the ratio σ/μ_b. On the other hand, we can attempt a fitting by fixing the intercept to be 1 per Eq. 7; the result is plotted as a solid line in Fig. 6. This fitting works as well, with a slightly decreased coefficient of determination, $R^2 = 0.64$. The ratio σ/μ_b is extracted to be 1490 μm. Its constancy suggests a strong regulating mechanism despite the changes in other properties. This we discuss in the next section.

Equations 3 and 4 allow us to extract the rheological properties (η, μ_b) based on the extracted timescales and measured value of σ for each aggregate type (using a standard technique following (8)). The results are summarized in Table 2 and shown in Fig. 7. In the figure, the three correlations, namely $\mu_b - \eta$, $\mu_b - \sigma$, and $\eta - \sigma$, are all approximately linear. The first and second are consequences of the relative constancy in τ_{long} (Fig. 4 *b*) and σ/μ_b, respectively. The third derives from the combination of the two. These results suggest that as the surface tension increases, bulk elasticity and viscosity also increase proportionally. The proportionality between surface tension and viscosity has also been observed in the long-time regime, in which an effective viscosity ($\sim 10^5$ Pa•s) due to cell rearrangements replaces η (20). The implications of these results are discussed in the next section.

TABLE 2 Extracted Bulk Elastic Modulus and Viscosity from Theory

Type	n	μ_b (Pa)	η (Pa•s)	E_{surf}/E_{bulk}
LN2a	23	1.55 ± 0.36	79.5 ± 24.9	31.6
LN4	18	2.93 ± 0.82	124 ± 35.4	22.8
3T3	31	18.6 ± 8.84	837 ± 449	30.1
Rat2	21	12.1 ± 3.40	570 ± 223	34.4
GBM −Dex	23	5.5 ± 0.97	168 ± 33.8	12.4
GBM +Dex	32	8.36 ± 1.42	347 ± 84.4	21.4
GBM −Dex +300Fn	31	5.30 ± 1.21	237 ± 104	14.9
GBM +Dex +300Fn	19	11.7 ± 3.85	359 ± 190	22.0
GBM DMSO	24	7.19 ± 2.70	345 ± 177	13.1
GBM PD03	31	7.92 ± 2.04	334 ± 95.8	19.2
GBM DMSO +300Fn	22	4.27 ± 1.16	147 ± 44.2	18.5
GBM PD03 +300Fn	15	22.5 ± 2.78	884 ± 155	19.4

The numbers represent mean and standard deviation, respectively.

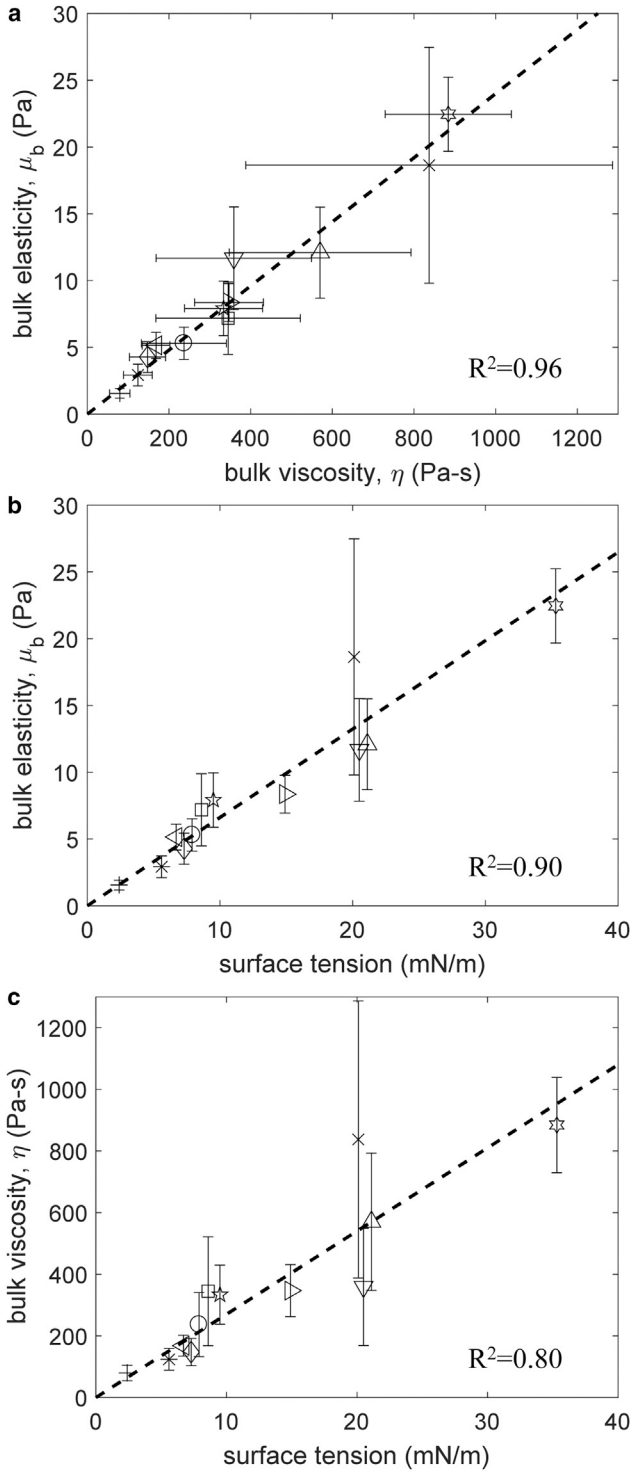

FIGURE 7 Extracted rheological properties: (*a*) bulk elasticity versus bulk viscosity; (*b*) bulk elasticity versus surface tension; and (*c*) bulk viscosity versus surface tension. In each graph, the dashed is a least-square-root fit in the form of $y = ax$. The same description of symbols from Fig. 4 applies. All error bars are SDs.

It is worthwhile to mention that the current model is one of the few we studied in (39) and is carefully selected based on both theoretical and experimental evaluations. For the

surface envelope, we choose to use a constant tension, σ. Other models, such as Gurtin-Murdoch and Helfrich-Canham, assume a variable surface tension, which is essentially nonlinear. Although a closed-form solution is not readily attained in these cases, they are not expected to follow a double-exponential behavior. The main competing and alternative model is hence the so-called "surface viscosity" model, which also assumes a constant surface tension. In this model, we replace the bulk viscosity, η, with a surface viscosity, η_s, assuming that the viscosity of the surface envelope is dominant. In this case, a solution with double-exponential relaxation is also attainable, and the reciprocals of timescales τ_{long}^{-1} and τ_{short}^{-1} are the real solutions to the following quadratic equation (39):

$$x^2 - \left(\frac{49}{8}\alpha' + 5\beta'\right)x + \frac{19}{4}\alpha'\left(\alpha' + \frac{20}{19}\beta'\right) = 0, \quad (8)$$

where $\alpha' = \mu_b R/\eta_s$, $\beta' = \sigma/\eta_s$. Although it does seem that this model can also be used to fit the relaxation data of individual aggregates equally well, the overall trend is opposite on the system level: the timescale ratio is linear to R (Fig. 8), not $1/R$ as shown in the data in Fig. 6. In addition, extraction of properties using this model leads to significant property scatter, e.g., two orders of magnitude variation in μ_b and η_s within the same aggregate type, and even negative values at times. The bulk viscosity model therefore is chosen to model the experimental system over the surface viscosity model, which also happens to be the simplest one consistently capturing the data following the philosophy of Occam's Razor.

DISCUSSION

The data presented in this study raise many interesting questions regarding the organization of multicellular tissue-like spheroid. Here, we attempt to discuss some of the implications.

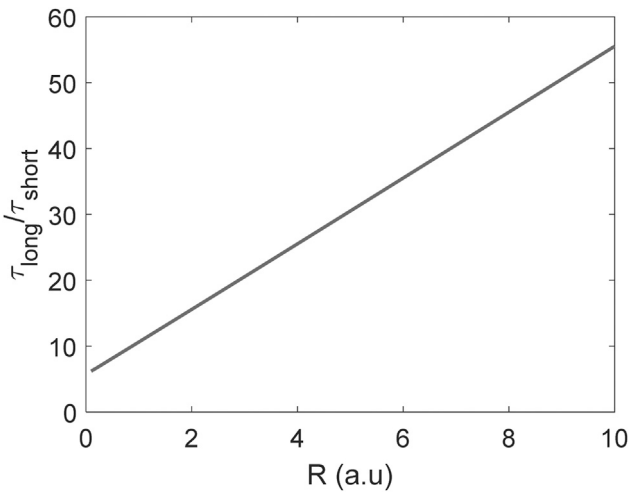

FIGURE 8 Relaxation timescale ratio plotted as a function of aggregate size as predicted by an alternative "surface viscosity" model.

Mechanical energy

The first is to realize that the ratio $\tau_{\text{long}}/\tau_{\text{short}}$ effectively represents the ratio of the total mechanical energy stored on the surface and in the bulk, because

$$\frac{E_{\text{surf}}}{E_{\text{bulk}}} \sim \frac{\sigma \times 4\pi R^2}{\mu_b \times (4/3)\pi R^3} = \frac{3\sigma}{\mu_b R} = \frac{57}{20}\left(\frac{\tau_{\text{long}}}{\tau_{\text{short}}} - 1\right). \quad (9)$$

The results are listed in Table 2 for each aggregate type. This ratio ranges from 12.4 for GBM −Dex to 34.4 for Rat2, demonstrating that the surface energy is in general one order of magnitude higher than the bulk energy. Consequently, during short-time deformation, the main energy change is also on the surface. Indeed, changes in energy follow a fixed ratio for an ellipsoidal deformation of any s_2,

$$\frac{\Delta E_{\text{surf}}}{\Delta E_{\text{bulk}}} = \frac{19}{15}\left(\frac{\tau_{\text{long}}}{\tau_{\text{short}}} - 1\right) = \frac{4}{9}\left(\frac{E_{\text{surf}}}{E_{\text{bulk}}}\right),$$

where Δ denotes the change from the original, spherical state (see Appendix C and Fig. 10 for derivative details). This conclusion is not surprising on the single-cell level: cells in the bulk in general are in a lower energy state due to intercellular adhesion, whereas the free (cell-medium) surface is in a higher energy state due to higher tension. This energy difference is simply the aggregate "surface tension." What is less intuitive, however, is that the overall energy on the aggregate surface is still much higher considering that the number of cells ($\sim(R/r)^2$, where r is the average radius of an individual cell) is typically an order of magnitude less than that in the bulk ($\sim(R/r)^3$). Together, we may estimate that the average mechanical energy per cell is two orders of magnitude lower in the interior than on the envelope. Note that here the mechanical energy (as well as the mechanical structure and forces discussed below) results from both active and passive responses of the cells. In addition, analysis above is used best for order-of-magnitude comparisons, as the properties used, such as μ_b, are bulk-averaged and do not capture the variability from cell to cell.

Mechanical structure

The same conclusion can be extrapolated to the mechanical structure: at the short timescales, the enveloping surface layer is mechanically much stronger than the interior. Because the T1 transition occurs with a characteristic velocity of $\sim$1.8 μm/min (20), an exchange of surface and interior cells typically occurs on the timescale of $\sim$10 min, much longer than the τ_{long} we measure. Hence in this case the surface layer is a well-defined mechanical enveloping

structure. The effective modulus of the surface envelope can be estimated as

$$\mu_s \sim \sigma/r \sim 10^3 \text{ Pa},$$

using $\sigma = 10$ mN/m and $r = 10$ μm. This modulus is also 2–3 orders of magnitude higher than μ_b. An equivalent gauge of surface envelope stiffness is the bending resistance, which can be approximately correlated with σ by the following formula (53):

$$\kappa \sim \sigma r^2/3 \sim 10^{-13} \text{ J}.$$

This value is much larger than that of a lipid membrane ($\sim 10^{-19}$J (54,55)). It is also evidently much stronger than that of a single-cell cortex as the tension is comparable (40,56), whereas the cortex thickness is orders of magnitude less ($\sim$100 nm) (57,58). It is particularly interesting to mention that the envelope is composed of identical units (cells) as those of the interior. The difference is entirely induced by cell-cell (and in some cases cell-ECM) adhesion. Note that in this argument, we assume the entire surface cell layer to be an entity and hence use the cell radius, r, as the length scale. In actuality, it is unclear what the mechanically "effective" thickness of the "surface envelope" is. This is a topic of future exploration.

Proportionality and cortical tension coregulation

The analysis above is made from the perspective of a tissue-level continuum model. In the following, we will discuss the possible cellular-level origin of such a "hard-envelope soft-interior" structure. Note that the strongest proportionality arises from Fig. 7 *b*, or equivalently Fig. 6. The ratio of σ/μ_b as extracted from Fig. 6 and using Eq. 7 is 1490 μm. This constant infers a proportionality between β_{cm}, cortical tension at the cell-medium interface (and on the aggregate envelope), and β_{cc}, cortical tension at cell-cell interfaces in the interior, which differs from β_{cm} because of cell-cell adhesion and cell-ECM adhesion. It is reasonable to propose that

$$\mu_b \sim \chi \frac{3\beta_{cc}}{r}.$$

Here, the factor of $3/r$ is the surface-to-volume ratio of a spherical cell, and the constant χ arises from other contributions including geometric factors. In other words, we assume that bulk elasticity arises from resistance of the individual cell cortices. On the other hand, to the leading order approximation $\sigma \sim \Delta\beta = \beta_{cm} - \beta_{cc}$, we therefore have

$$\beta_r = \beta_{cc}/\beta_{cm} \sim 0.002\chi^{-1}, \tag{10}$$

again using $r = 10$ μm, and that $\sigma/\mu_b = 1490$ μm. This proportionality is indeed supported by observations of David et al. for non-drug-treated tissue: all of σ, β_{cm}, and β_{cc} increase proportionally (see Table 1 in (20), wherein β and T correspond to β_{cm} and β_{cc}, respectively) for *Xenopus* explants. On the other hand, the ratio β_r ranges from 0.26 to 0.44 for untreated tissues in (20). If we were to apply these numbers to our study, we will obtain an unusually low χ on the order of 10^{-2}. This result is inconsistent, as although several factors including annealing and geometric shape may contribute to a lesser value, it should not deviate from 1 by more than one order of magnitude. Instead, we speculate that β_r in our study is indeed small, and the discrepancy with (20) can be explained by 1) the species (*Xenopus* versus mammalian) are different; 2) that β_r in (20) was measured with the adhesion dynamics of a pair of suspended cells not in contact with others, whereas further adhesion with multiple surrounding cells, especially of those in the interior which have no "free" interface, may further and significantly reduce β_{cc} and weaken β_r; 3) that the surface tensions in this study are in general one to two orders of magnitude greater than those in (20); and 4) the spheroids used in this study are developed for 48 h, as opposed to a few hours in (20). The second point above could be due to the nonlinear nature of tension-adhesion coupling, and exemplary models are found in (23,36,59). Overall, a tension ratio on the order of 10^{-3} indicates a strong reduction in cell-cell tension, which approaches the "flabby" state (23,59). Experimentally, this is supported by the observation of the actin cortices by Krieg et al. (40).

The proportionality between surface tension and viscosity is also observed by David et al. but on the much longer rearrangement timescale (hours) (20). In this case, the effective viscosity, η_{rea} (where the subscript denotes "rearrangement" to distinguish from η in the current work) scales linearly with σ across a 10-fold change in the latter. This linearity is caused by a constant rearrangement velocity of $\sim$1.8 μm/min, which arises from the dynamics of cell-cell adhesion, and which is conserved across different cell types. In contrast to the much greater values of η_{rea} (several to tens of kPa•s), the viscosity (tens to hundreds of Pa•s) in the current work is much weaker and of a different origin. It most likely represents the effects of both cytoplasmic and cortical dissipation, with the latter being dominant (60).

Most notably, this study and prior work by David et al. (20) arrive at the proportionality between β_{cc} and β_{cm} through completely different approaches and on very different timescales. In (20) and deriving from a theory by Marmottant et al. (19), the authors arrive at a scaling relationship of $\eta_{rea} \sim \beta_{cc}$. Further considering $\sigma \sim \beta_{cm} - \beta_{cc}$ and the experimental measured linearity between σ and η_{rea} leads to the necessary proportionality among all three tensions, which is also supported via contact angle measurement of the cell pair. In the current work, the proportionality arises from that between σ and μ_b, obtained via timescales τ_{long} and τ_{short}, which are much shorter than that for aggregate rounding. If surface tension is indeed controlled by

adhesion, which is most directly indicated in (42), then we may speculate that adhesion simultaneously upregulates both cortical tensions. Note that this is not contradictory to or to be confused with the downregulation of cortical tension at the cell-cell contact, which is simply to say, $\beta_{cc} < \beta_{cm}$. Our main hypothesis from the current work is that increased adhesion leads to an increase in β_{cm} in a manner similar to cells attached to a substrate (61,62), meanwhile "leaving" a higher β_{cc} (relative to β_{cm} or a higher β_r) at the cell-cell contact. Furthermore, this process is regulated in a precise manner to maintain the proportionality and the constancy in the relaxation times. The physical mechanism for the proportionality between bulk viscosity and β_{cc} (β_{cm}), on the other hand, is unknown. However, if we assume bulk viscosity mainly arises from the viscosity of the cortices and the interstitial fluids between cells, such a trend is not surprising. Although direct studies are lacking, literature investigating analogous situation in molecular contacts does suggest that increased adhesion leads to increased "friction" (63).

Coherent timescales in multicellular aggregation

A multicellular aggregate is a complex, hierarchical structure that involves organization on multiple length scales, from subcellular to the tissue level. A wide range of timescales also emerges, corresponding to the dynamic processes (12,38). The two timescales observed here arise from the collective, short-time response of the cells. The timescale observed in (20), on the other hand, owes to the long-time rearrangement of cells.

The constancy in the timescales and ratios reflects the precise regulation of the underlying cellular properties. In an earlier study by one of us (R.A.F. (50), Table 1 therein), similar timescales in aggregates of chick embryo origin were also observed, in which the short timescale was around 2 s and the long 22.5–44.8 s. Although these values are somewhat lower than our measurements on mammalian tissues, they are of the same order of magnitude. Interestingly, such timescales (seconds and minutes) were also present in calcium-signaling dynamics in the context of wound healing and mechanical loading in *Drosophila* wings, although it is not clear whether they are related to those in the current observation (64,65). Apparently, multicellular organizations preserve these timescales, whereas other properties can vary more drastically. The fundamental cause for this preservation, as well as the proposed coregulation of cell-medium and cell-cell tensions, requires further study.

In perspective, we introduce what is to our knowledge a new approach—namely, ellipsoidal relaxation analysis—to measure tissue mechanical properties. The results have significant implications to the study of morphogenesis and tumor biology. Indeed, various studies have previously demonstrated a clear role for tissue mechanical properties in controlling important morphological events, including blastopore (66) and neural tube closure (67) in amphibians and gastrulation in amphibians (68) and fish (23), as well as heart tube assembly in chicks (69). These studies, however, were for the most part performed using methods that do not adequately model the tissue and essentially neglect the relationship between the elastic properties of surface and bulk cells. Our method is able to differentiate these properties and may provide important clues as to how changes in cell stiffness impact the overall mechanical properties of the bulk tissue. Tissue mechanical properties have also been used in imaging modalities such as magnetic resonance elastography to identify changes in the malignant properties of brain tissue in murine models (70) and in the brain (71,72) and liver (73) of human patients. These methods are also quite informative, but require use of very expensive equipment and do not easily lend themselves to experimental manipulation of tumor tissue. Our in vitro method is relatively straightforward and can be easily modified to incorporate chemotherapy and other agents to determine their effects on tumor mechanical properties and to allow us to ultimately connect changes in stiffness or viscosity to their molecular determinants.

APPENDIX A: VOLUME VERIFICATION AND 3D SHAPE EXTRAPOLATION

We assume an axisymmetric oblate shape for aggregate. This assumption is verified by tracking volume change during shape relaxation. A typical volume evolution as calculated from Eq. 1 is shown in Fig. 9. The near-constant volume (0.5% fluctuation) verifies our approach of extrapolating the 3D shape from the 2D imaging.

APPENDIX B: ANALYSIS OF THE $l = 4$ MODE

Solution to the $l = 4$ mode provides

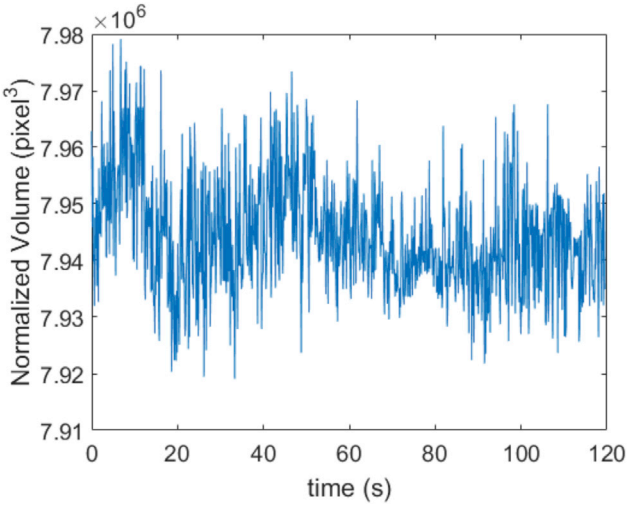

FIGURE 9 Exemplary aggregate GBM with DMSO volume evolution during shape relaxation. To see this figure in color, go online.

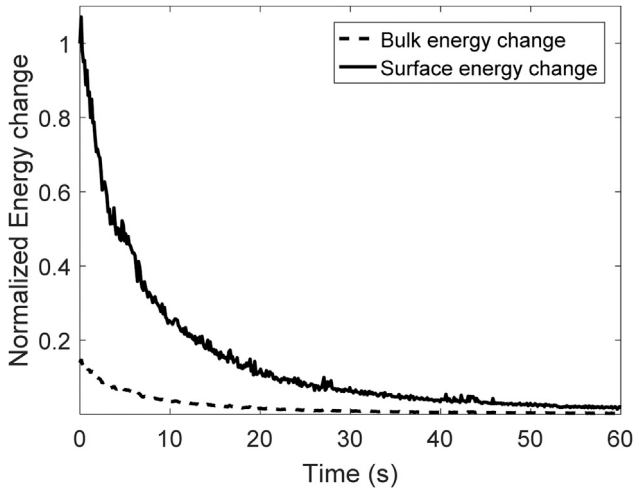

FIGURE 10 Evolution of estimated mechanical energy stored in bulk ΔE_{bulk} and on surface ΔE_{surf}, following Eq. 13 and data in Fig. 1 *b*. The energies are normalized by ΔE_{surf} at the beginning of relaxation. $\sigma = 8.6$ mN/m, $\mu_b = 5.16$ Pa, and $R = 308.2$ μm.

$$\tau_{\text{short}}^{l=4} = \left(\frac{36}{17}\frac{1}{\tau_1} + \frac{1}{\tau_2}\right)^{-1}, \quad \tau_{\text{long}}^{l=4} = \tau_2. \tag{11}$$

This is the second dominant mode next to $l = 2$ in our experiments. The signal to noise ratio for this mode is generally not amenable to meaningful analysis in most experiments. However, occasionally, reasonable results can be achieved. One example is provided here. Analysis of the 24 GBM DMSO aggregates reveals $\tau_{\text{short}}^{l=4} = 5.2 \pm 3.4$ s and $\tau_{\text{long}}^{l=4} = 41.2 \pm 32.5$ s, compared with $\tau_{\text{short}}^{l=2} = 8.4 \pm 3.3$ s and $\tau_{\text{long}}^{l=2} = 46.9 \pm 11.3$ s. Based on these timescales, the mean values for τ_1 and τ_2 (the physical timescales as defined by Eq. 4) are as follows:

$$\tau_1 = 10.6 \text{ s}, \quad \tau_2 = 46.9 \text{ s}$$

from the $l = 2$ analysis and

$$\tau_1 = 12.6 \text{ s}, \quad \tau_2 = 41.2 \text{ s}$$

from the $l = 4$ analysis. The sets of values are very similar, although with some expected deviations. This exercise attests to the consistency and validity of the current theory. However, note that in general, the standard deviation in the $l = 4$ analysis is much higher due to the lower signal-to-noise ratio.

APPENDIX C: THEORETICAL EVALUATION OF ENERGY CHANGE DURING ELLIPSOIDAL DEFORMATION

The mechanical energy stored in bulk, E_{bulk}, and on the surface layer, E_{surf}, upon deformation (and during natural relaxation) is evaluated by the formulae

$$\Delta E_{\text{bulk}} = \int \mu_b \nabla \mathbf{u} \cdot \nabla \mathbf{u} \mathrm{d}V, \; \Delta E_{\text{surf}} = \int \sigma \mathrm{d}A, \tag{12}$$

respectively, where V is the volume, and A is the total surface area. The moduli μ_b and σ are considered constants to the leading-order accuracy. In general, the displacement field $\mathbf{u}$ has to be known everywhere in the aggregate to calculate ΔE_{bulk} and ΔE_{surf}. Such information is not available with the experimental setup of the current study. However, without losing generality, scaling analysis can still be performed using the measured evolution of s_2. We assume that the radial displacement field u_r is linearly distributed with respect to r, and the tangential displacement u_θ is temporarily ignored. Then the following result can be obtained with $u_r(r, \theta) = s_2 r P_2(\cos\theta)$:

$$\Delta E_{\text{bulk}} = \frac{18}{15}\pi\mu_b s_2^2 R^3, \; \Delta E_{\text{surf}} = \frac{8}{5}\pi\sigma s_2^2 R^2, \tag{13}$$

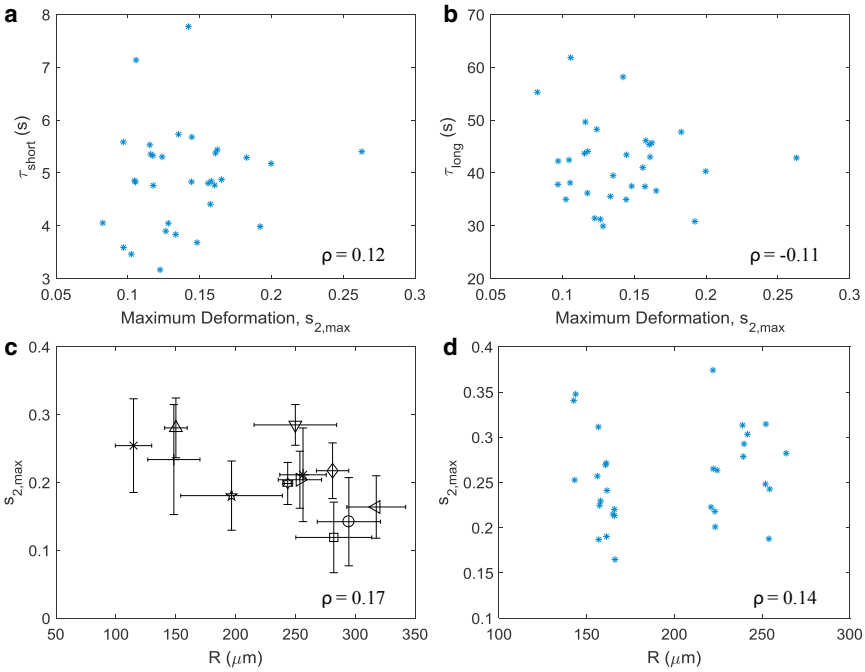

FIGURE 11 (*a* and *b*) Relaxation timescales plotted versus maximal deformation in s_2, $s_{2,\max}$ for GBM +Dex. The Pearson correlation coefficient, ρ, is 0.12 and −0.11, respectively. (*c*) The mean $s_{2,\max}$ is plotted as a function of R for all aggregate types. The same description of symbols from Fig. 4 applies. All error bars are SDs. The Pearson correlation coefficient, ρ, is 0.17 (*d*) $s_{2,\max}$ is plotted as a function of R for GBM PD03. The Pearson correlation coefficient, ρ, is 0.14. To see this figure in color, go online.

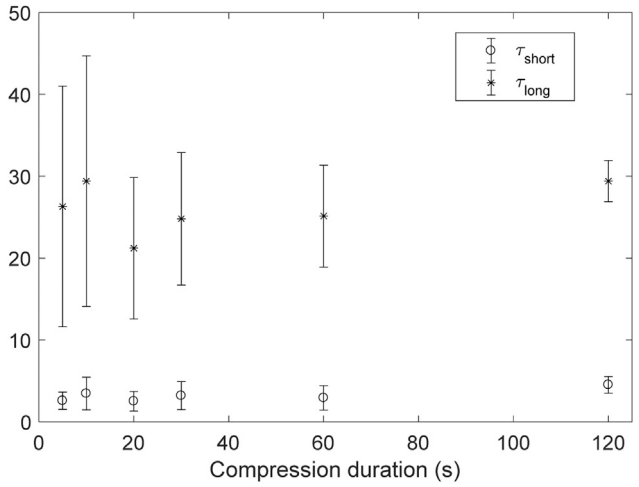

FIGURE 12 Relaxation timescales versus compression duration for GBM2 aggregates ($n = 9$). The same aggregate was subsequently subject to compression for 5, 10, 20, 30, 60, and 120 s in duration. Error bars are SDs.

which leads to

$$\frac{\Delta E_{surf}}{\Delta E_{bulk}} = \frac{4}{3}\frac{\sigma}{\mu_b R} = \frac{19}{15}\left(\frac{\tau_{long}}{\tau_{short}} - 1\right). \quad (14)$$

For the timescale ratios listed in Table 1, Eq. 14 suggests that ΔE_{surf} dominates over ΔE_{bulk} by an order of magnitude. This is illustrated in Fig. 10, which is evaluated via Eq. 13 using the s_2 data in Fig. 1 *b* and $\sigma = 8.6$ mN/m, $\mu_b = 5.16$ Pa, and $R = 308.2$ μm, all extracted for this particular case. Note that the energy changes are normalized by ΔE_{surf} at $t = 0$.

APPENDIX D: DEPENDENCE OF TIMESCALES ON THE DEGREE AND DURATION OF COMPRESSION

No dependence of the timescales on the degree and duration of compression was detected as demonstrated in Figs. 11 and 12. In Fig. 11, *a* and *b*, both τ_{short} and τ_{long} are plotted against the maximal mode amplitude, $s_{2,max}$, for GBM +Dex ($n = 32$). Pearson's correlation coefficients are 0.12 and −0.11, respectively, indicating very weak correlation. This behavior is representative for all types we studied. The aggregate radius, R, also shows no apparent correlation with $s_{2,max}$. The result is shown for mean values of each aggregate type in Fig. 11 *c* (Pearson's correlation coefficient is 0.17) and for each compression for one aggregate type (GBM PD03) in Fig. 11 *d* (Pearson's correlation coefficient is 0.14).

In Fig. 12, GBM2 aggregates were subject to compression duration of 5–120 s. The results demonstrate that these timescales generally have weak to no apparent dependence on how long the aggregates are subject to compression. Hence, we choose 30 s as the compression time for all experiments performed in the proper text without losing generality.

SUPPORTING MATERIAL

One video is available at http://www.biophysj.org/biophysj/supplemental/S0006-3495(18)30496-X.

AUTHOR CONTRIBUTIONS

H.L., R.A.F., and M.Y. conceived the idea and designed the experiments. A.M., P.B., and Y.D. prepared the samples and performed the experiments. M.Y., H.L., and L.L. performed theoretical development, data analysis, and model and hypothesis validation. M.Y., H.L., and R.A.F. wrote and revised the manuscript. All authors participated in discussion and manuscript development.

REFERENCES

1. Mueller-Klieser, W. 1987. Multicellular spheroids. A review on cellular aggregates in cancer research. *J. Cancer Res. Clin. Oncol.* 113:101–122.
2. Kunz-Schughart, L. A. 1999. Multicellular tumor spheroids: intermediates between monolayer culture and in vivo tumor. *Cell Biol. Int.* 23:157–161.
3. Lin, R. Z., and H. Y. Chang. 2008. Recent advances in three-dimensional multicellular spheroid culture for biomedical research. *Biotechnol. J.* 3:1172–1184.
4. Mironov, V., R. P. Visconti, …, R. R. Markwald. 2009. Organ printing: tissue spheroids as building blocks. *Biomaterials.* 30:2164–2174.
5. Foty, R. A., and M. S. Steinberg. 2013. Differential adhesion in model systems. *Wiley Interdiscip. Rev. Dev. Biol.* 2:631–645.
6. Au, S. H., B. D. Storey, …, M. Toner. 2016. Clusters of circulating tumor cells traverse capillary-sized vessels. *Proc. Natl. Acad. Sci. USA.* 113:4947–4952.
7. Steinberg, M. S. 1963. Reconstruction of tissues by dissociated cells. Some morphogenetic tissue movements and the sorting out of embryonic cells may have a common explanation. *Science.* 141: 401–408.
8. Foty, R. A., G. Forgacs, …, M. S. Steinberg. 1994. Liquid properties of embryonic tissues: measurement of interfacial tensions. *Phys. Rev. Lett.* 72:2298–2301.
9. Foty, R. A., C. M. Pfleger, …, M. S. Steinberg. 1996. Surface tensions of embryonic tissues predict their mutual envelopment behavior. *Development.* 122:1611–1620.
10. Davis, G. S., H. M. Phillips, and M. S. Steinberg. 1997. Germ-layer surface tensions and "tissue affinities" in Rana pipiens gastrulae: quantitative measurements. *Dev. Biol.* 192:630–644.
11. Beysens, D. A., G. Forgacs, and J. A. Glazier. 2000. Cell sorting is analogous to phase ordering in fluids. *Proc. Natl. Acad. Sci. USA.* 97:9467–9471.
12. Gonzalez-Rodriguez, D., K. Guevorkian, …, F. Brochard-Wyart. 2012. Soft matter models of developing tissues and tumors. *Science.* 338:910–917.
13. Takeichi, M. 1988. The cadherins: cell-cell adhesion molecules controlling animal morphogenesis. *Development.* 102:639–655.
14. Hardin, J. 1989. Local shifts in position and polarized motility drive cell rearrangement during sea urchin gastrulation. *Dev. Biol.* 136: 430–445.
15. Foty, R. A., and M. S. Steinberg. 2004. Cadherin-mediated cell-cell adhesion and tissue segregation in relation to malignancy. *Int. J. Dev. Biol.* 48:397–409.
16. Pegoraro, A. F., J. J. Fredberg, and J. A. Park. 2016. Problems in biology with many scales of length: cell-cell adhesion and cell jamming in collective cellular migration. *Exp. Cell Res.* 343: 54–59.
17. Phillips, H. M., and M. S. Steinberg. 1978. Embryonic tissues as elasticoviscous liquids. I. Rapid and slow shape changes in centrifuged cell aggregates. *J. Cell Sci.* 30:1–20.
18. Brodland, G. W. 2003. New information from cell aggregate compression tests and its implications for theories of cell sorting. *Biorheology.* 40:273–277.
19. Marmottant, P., A. Mgharbel, …, H. Delanoë-Ayari. 2009. The role of fluctuations and stress on the effective viscosity of cell aggregates. *Proc. Natl. Acad. Sci. USA.* 106:17271–17275.

20. David, R., O. Luu, …, R. Winklbauer. 2014. Tissue cohesion and the mechanics of cell rearrangement. *Development.* 141:3672–3682.

21. Graner, F., and J. A. Glazier. 1992. Simulation of biological cell sorting using a two-dimensional extended Potts model. *Phys. Rev. Lett.* 69: 2013–2016.

22. Graner, F. 1993. Can surface adhesion drive cell-rearrangement? Part I: biological cell sorting. *J. Theor. Biol.* 164:455–476.

23. Manning, M. L., R. A. Foty, …, E. M. Schoetz. 2010. Coaction of intercellular adhesion and cortical tension specifies tissue surface tension. *Proc. Natl. Acad. Sci. USA.* 107:12517–12522.

24. Schötz, E. M., M. Lanio, …, M. L. Manning. 2013. Glassy dynamics in three-dimensional embryonic tissues. *J. R. Soc. Interface.* 10: 20130726.

25. Guillot, C., and T. Lecuit. 2013. Mechanics of epithelial tissue homeostasis and morphogenesis. *Science.* 340:1185–1189.

26. Hayashi, T., and R. W. Carthew. 2004. Surface mechanics mediate pattern formation in the developing retina. *Nature.* 431:647–652.

27. Jakab, K., B. Damon, …, G. Forgacs. 2008. Relating cell and tissue mechanics: implications and applications. *Dev. Dyn.* 237:2438–2449.

28. Merkel, M., and M. L. Manning. 2016. Using cell deformation and motion to predict forces and collective behavior in morphogenesis. *Semin. Cell Dev. Biol.* 67:161–169.

29. Mombach, J. C. M., D. Robert, …, J.-P. Rieu. 2005. Rounding of aggregates of biological cells: experiments and simulations. *Physica A.* 352:525–534.

30. Farhadifar, R., J. C. Röper, …, F. Jülicher. 2007. The influence of cell mechanics, cell-cell interactions, and proliferation on epithelial packing. *Curr. Biol.* 17:2095–2104.

31. Forgacs, G., and I. Kosztin. 2010. Cellular aggregates under pressure. *Physics (College Park Md.).* 3:43.

32. Guevorkian, K., M. J. Colbert, …, F. Brochard-Wyart. 2010. Aspiration of biological viscoelastic drops. *Phys. Rev. Lett.* 104:218101.

33. Staple, D. B., R. Farhadifar, …, F. Jülicher. 2010. Mechanics and remodelling of cell packings in epithelia. *Eur. Phys. J. E Soft Matter.* 33:117–127.

34. Bi, D., J. H. Lopez, …, M. L. Manning. 2014. Energy barriers and cell migration in densely packed tissues. *Soft Matter.* 10:1885–1890.

35. Fletcher, A. G., M. Osterfield, …, S. Y. Shvartsman. 2014. Vertex models of epithelial morphogenesis. *Biophys. J.* 106:2291–2304.

36. Bi, D., J. H. Lopez, …, M. L. Manning. 2015. A density-independent rigidity transition in biological tissues. *Nat. Phys.* 11:1074–1079.

37. Barton, D. L., S. Henkes, …, R. Sknepnek. 2017. Active Vertex Model for cell-resolution description of epithelial tissue mechanics. *PLoS Comput. Biol.* 13:e1005569.

38. Pajic-Lijakovic, I., and M. Milivojevic. 2017. Successive relaxation cycles during long-time cell aggregate rounding after uni-axial compression. *J. Biol. Phys.* 43:197–209.

39. Liu, L., M. Yu, …, R. A. Foty. 2017. Deformation and relaxation of an incompressible viscoelastic body with surface viscoelasticity. *J. Mech. Phys. Solids.* 98:309–329.

40. Krieg, M., Y. Arboleda-Estudillo, …, C. P. Heisenberg. 2008. Tensile forces govern germ-layer organization in zebrafish. *Nat. Cell Biol.* 10:429–436.

41. Nose, A., A. Nagafuchi, and M. Takeichi. 1988. Expressed recombinant cadherins mediate cell sorting in model systems. *Cell.* 54:993–1001.

42. Foty, R. A., and M. S. Steinberg. 2005. The differential adhesion hypothesis: a direct evaluation. *Dev. Biol.* 278:255–263.

43. Shannon, S., C. Vaca, …, R. A. Foty. 2015. Dexamethasone-mediated activation of fibronectin matrix assembly reduces dispersal of primary human glioblastoma cells. *PLoS One.* 10:e0135951.

44. Mehta, M., A. Khan, …, H. E. Sabaawy. 2015. Radiosensitization of primary human glioblastoma stem-like cells with low-dose AKT inhibition. *Mol. Cancer Ther.* 14:1171–1180.

45. Shannon, S., D. Jia, …, R. A. Foty. 2017. Inhibition of glioblastoma dispersal by the MEK inhibitor PD0325901. *BMC Cancer.* 17:121.

46. Caicedo-Carvajal, C. E., T. Shinbrot, and R. A. Foty. 2010. $\alpha 5\beta 1$ integrin-fibronectin interactions specify liquid to solid phase transition of 3D cellular aggregates. *PLoS One.* 5:e11830.

47. Foty, R. 2011. A simple hanging drop cell culture protocol for generation of 3D spheroids. *J. Vis. Exp.* 51:e2720.

48. Meleis, A. M., A. Mahtabfar, …, R. A. Foty. 2017. Dexamethasone-mediated inhibition of Glioblastoma neurosphere dispersal in an ex vivo organotypic neural assay. *PLoS One.* 12:e0186483.

49. Tjahjadi, M., J. M. Ottino, and H. A. Stone. 1994. Estimating interfacial tension via relaxation of drop shapes and filament breakup. *AlChE J.* 40:385–394.

50. Forgacs, G., R. A. Foty, …, M. S. Steinberg. 1998. Viscoelastic properties of living embryonic tissues: a quantitative study. *Biophys. J.* 74:2227–2234.

51. Guido, S., and M. Villone. 1999. Measurement of interfacial tension by drop retraction analysis. *J. Colloid Interface Sci.* 209:247–250.

52. Roylance, D. 2001. Engineering viscoelasticity. http://web.mit.edu/course/3/3.11/www/modules/visco.pdf.

53. Marsh, D. 2006. Elastic curvature constants of lipid monolayers and bilayers. *Chem. Phys. Lipids.* 144:146–159.

54. Dimova, R. 2014. Recent developments in the field of bending rigidity measurements on membranes. *Adv. Colloid Interface Sci.* 208:225–234.

55. Yu, M., R. B. Lira, …, H. Lin. 2015. Ellipsoidal relaxation of deformed vesicles. *Phys. Rev. Lett.* 115:128303.

56. Evans, E., and A. Yeung. 1989. Apparent viscosity and cortical tension of blood granulocytes determined by micropipet aspiration. *Biophys. J.* 56:151–160.

57. Charras, G. T., C. K. Hu, …, T. J. Mitchison. 2006. Reassembly of contractile actin cortex in cell blebs. *J. Cell Biol.* 175:477–490.

58. MacQueen, L. A., M. Thibault, …, M. R. Wertheimer. 2012. Electromechanical deformation of mammalian cells in suspension depends on their cortical actin thicknesses. *J. Biomech.* 45:2797–2803.

59. Kim, S., and S. Hilgenfeldt. 2015. Cell shapes and patterns as quantitative indicators of tissue stress in the plant epidermis. *Soft Matter.* 11:7270–7275.

60. Bausch, A. R., W. Möller, and E. Sackmann. 1999. Measurement of local viscoelasticity and forces in living cells by magnetic tweezers. *Biophys. J.* 76:573–579.

61. Discher, D. E., P. Janmey, and Y. L. Wang. 2005. Tissue cells feel and respond to the stiffness of their substrate. *Science.* 310:1139–1143.

62. Wang, C., S. Chowdhury, …, W. Losert. 2014. The interplay of cell-cell and cell-substrate adhesion in collective cell migration. *J. R. Soc. Interface.* 11:20140684.

63. Busuttil, K., M. Geoghegan, …, G. J. Leggett. 2011. Contact mechanics of nanometer-scale molecular contacts: correlation between adhesion, friction, and hydrogen bond thermodynamics. *J. Am. Chem. Soc.* 133:8625–8632.

64. Shannon, E. K., A. Stevens, …, M. S. Hutson. 2017. Multiple mechanisms drive calcium signal dynamics around laser-induced epithelial wounds. *Biophys. J.* 113:1623–1635.

65. Narciso, C. E., N. M. Contento, …, J. J. Zartman. 2017. Release of applied mechanical loading stimulates intercellular calcium waves in Drosophila wing discs. *Biophys. J.* 113:491–501.

66. Feroze, R., J. H. Shawky, …, L. A. Davidson. 2015. Mechanics of blastopore closure during amphibian gastrulation. *Dev. Biol.* 398:57–67.

67. Zhou, J., H. Y. Kim, and L. A. Davidson. 2009. Actomyosin stiffens the vertebrate embryo during crucial stages of elongation and neural tube closure. *Development.* 136:677–688.

68. von Dassow, M., and L. A. Davidson. 2009. Natural variation in embryo mechanics: gastrulation in Xenopus laevis is highly robust to variation in tissue stiffness. *Dev. Dyn.* 238:2–18.

69. Varner, V. D., and L. A. Taber. 2012. Not just inductive: a crucial mechanical role for the endoderm during heart tube assembly. *Development.* 139:1680–1690.

70. Schregel, K., N. Nazari, …, S. Patz. 2017. Characterization of glioblastoma in an orthotopic mouse model with magnetic resonance elastography. *NMR Biomed* Published online November 29, 2017. https://doi.org/10.1002/nbm.3840.

71. Chauvet, D., M. Imbault, …, M. Tanter. 2016. In vivo measurement of brain tumor elasticity using intraoperative shear wave elastography. *Ultraschall Med.* 37:584–590.

72. Reiss-Zimmermann, M., K. J. Streitberger, …, K. T. Hoffmann. 2015. High resolution imaging of viscoelastic properties of intracranial tumours by multi-frequency magnetic resonance elastography. *Clin. Neuroradiol.* 25:371–378.

73. Grgurevic, I., T. Bokun, …, A. Berzigotti. 2017. Liver elastography malignancy prediction score for noninvasive characterization of focal liver lesions. *Liver Int* Published online November 3, 2017. https://doi.org/10.1111/liv.13611.